

Compact High Performance Hybrid Reluctance Actuated Fast Steering Mirror System

E. Csencsics^a, J. Schlarp^a, T. Schopf^{fb}, G. Schitter^a

^aChristian Doppler Laboratory for Precision Engineering for Automated In-Line Metrology at the Automation and Control Institute, Technische Universität Wien, A-1040 Vienna, Austria.

^bEddy Current Sensors Division at Micro-Epsilon Messtechnik GmbH, Königbacherstrasse 15, 94496 Ortenburg, Germany.

Abstract

This work presents the design, analysis, control and evaluation of a novel compact and highly integrated fast steering mirror (FSM) system, which is based on a hybrid reluctance tip/tilt actuator. The actuator design employs a permanent magnet for biasing the magnet circuit with a constant flux and two pairs of coils to generate a steering flux for rotating the mover around the two system axes. The system, designed to be used as scanning unit in compact optical metrology systems, uses a custom made eddy current sensor system for position measurement and a titanium flexure, which compensates the negative actuator stiffness, for suspending the mover. The FSM provides a mechanical angular range of $\pm 3^\circ$ (± 52.4 mrad) and a small signal closed-loop bandwidth of 1.5 kHz in the tip and tilt axis, has a small diameter of 32 mm and a system height of only 30 mm. Compared to a state-of-the-art hybrid reluctance actuated FSM system the volume of the system is reduced by one order of magnitude, while the product of range times bandwidth, representing a measure for the system performance, is concurrently improved by 50%.

Keywords: Fast steering mirror, Hybrid reluctance actuation, Flux steering, Flexure Design, Tip/tilt system

1. Introduction

Fast steering mirrors (FSMs) are opto-mechatronic devices that are used within various scientific applications, which can be divided into scanning and pointing applications. Typical scanning applications are widely spread and include systems for confocal microscopy [1], scanning optical lithography [2], material processing [3] and laser scanners [4]. Pointing applications range from line of sight stabilization in optical systems, such as in optical free space communication [5], over acquisition of optical signals and tracking of objects [6] to pointing of laser or light beams on a target [7]. FSMs are most commonly actuated by either piezo [8] or voice coil [4] actuators. Piezo actuators are used for high stiffness systems with higher bandwidth but limited range, such as ± 2 mrad and 1 kHz [5], while voice coil actuators are typically used to design low stiffness systems with larger scan range but limited bandwidth, such as ± 87 mrad and 350 Hz [7]. From the reported FSM systems it is apparent that there is a performance tradeoff required at the stage of system design, as large bandwidth and large range are competing requirements and can not be achieved at the same time.

In order to relax this tradeoff, actuators based on reluctance force are a promising alternative, as they provide larger ranges than piezos and have higher motor constants than voice coil actuators [9]. But they come along with several challenges, such as the ability to exert only unidirectional forces [10] or the non-linear force-to-current and force-to-gap size relations [11]. Additional aspects like ferromagnetic hysteresis [12] make an accurate modeling of the reluctance challenging [13], which may be the reason that they have

Email address: csencsics@acin.tuwien.ac.at (E. Csencsics)

Preprint submitted to IFAC Mechatronics

December 11, 2019

hardly been applied to high precision scanning and positioning systems for a long time. In recent years, however, several designs of mechatronic systems, which are actuated based on reluctance principles, have been developed in order to exploit the benefits of this technology. A design study, presenting the concept of a variable reluctance actuated FSM [14], has been reported, promising a range of $\pm 1^\circ$ and a targeted bandwidth of 1 kHz. A high force linear hybrid reluctance (HR) actuator, using a permanent magnet for linearization, with a range of ± 1 mm and low stiffness has been developed for the active vibration isolation in precision machines [15]. The term hybrid thereby refers to the use of two different sources of magnetic flux (coils and permanent magnets). More compact reluctance actuators with short strokes around 100 μm are designed for linear actuation within fast tool servos [16, 17] and valve engines [18]. Reluctance actuators have also been employed to enable rotational motion in FSM systems. A FSM with an angular range of ± 3.5 mrad is reported to achieve a closed-loop system bandwidth of 2 kHz with internal sensors and 10 kHz with a fast external optical sensor system [19]. The system uses four HR actuators, with distinct magnetic circuits and biasing magnets, placed around the mover, which leads to system dimensions of 65 x 65 x 40 mm. Design studies of more compact FSM system with comparable angular range are also reported but have not been realized so far [20, 21]. Recently also the concept of a HR tip/tilt-actuator has been developed, which integrates the distinct actuators into a single one [22]. It enables larger angular range of motion while still obtaining a bandwidth of 1 kHz but is still rather bulky with an outer diameter of 100 mm and a height of 70 mm.

A common disadvantage of all these HR actuated systems is their size, which is either caused by the size and number of actuators or the low level of system integration. The system dimensions are a key property when it comes to the integration of FSMs into compact optical systems, such as in scanning laser metrology [23], projection systems or optical inter-satellite communication [24]. This paper presents the first

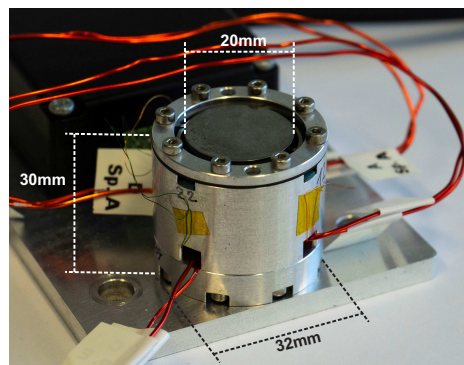


Figure 1: Photograph of the compact hybrid reluctance actuated fast steering mirror system. The system is 30 mm high and has a diameter of 32 mm, with a mirror diameter of 20 mm.

implementation of a compact and highly integrated FSM system actuated by an HR tip/tilt actuator [22] (see Fig. 1). With dimensions of $\phi 32 \times 30$ mm it is suited for the use in compact optical systems that require small scanners for beam steering and provides a large angular range of $\pm 3^\circ$ (± 52.4 mrad) mechanical. The compact design, the system integration and the actual construction bring along several challenges. This includes appropriate material and design choices for yoke parts and the combined suspension system, the integrated mover design and the placement and shape of position sensors. Solutions to these challenges are addressed throughout the paper and represent its main contribution, together with the system integration and the analysis of the system dynamics. The target specifications of the compact FSM system, summarized in Table 1, are obtained based on a thorough literature review of reported tip/tilt system specifications, typical requirements of the targeted scanning applications in optical metrology systems and the aim to design the most compact large range FSM system available. The mover shall accommodate mirrors up to 20 mm and has thus a diameter of 20 mm. To still provide a sinusoidal scan amplitude of at least 1 mrad

at 1 kHz, a maximum angular acceleration of $4 \times 10^4 \text{ rad/s}^2$ is targeted.

Table 1: Performance goals of compact FSM.

Parameter	Performance goal
Angular range	$\pm 3^\circ$
Dimensions	30 x 30 mm
Mover diameter	20 mm
Bandwidth	1 kHz
Angular acceleration	$4 \times 10^4 \text{ rad/s}^2$

The design of the compact FSM system with a system overview, the working principle of the actuator and the actuator dimensioning is discussed in Sections 2.1 to 2.3. In Section 2.4 the mechanical suspension system is described and a parametrized model of the system dynamics is obtained in Section 2.6. Section 3 discusses the implementation of the designed system and the controller design and is followed by the experimental evaluation of the system performance in Section 4. Section 5 concludes the paper.

2. Compact FSM Design

2.1. System Overview

The proposed compact FSM system is based on an HR actuator design with two rotational degrees of freedom [22]. The actuation principle relies on the strengthening and weakening of a biasing field in two opposing air gaps, which is generated by a permanent magnet. The motor constant of the actuator is linearized by this permanent magnetic biasing field and is higher compared to a voice coil actuator with the same level of dissipated power [16, 9]. The system design enables to place all system components behind the mirror surface, such that the field of view is not obstructed, and puts the point of rotation only single millimeters behind the mirror plane. As no additional actuator components need to be attached to the moving part, as it would be necessary for voice coil actuators (magnetic circuit), the inertia of the mover can be kept minimal with respect to structural considerations.

Fig. 2 shows a CAD rendering of the compact FSM system providing an overview of the main components of the system. The entire system is housed in a solid aluminium body, providing sufficient stiffness

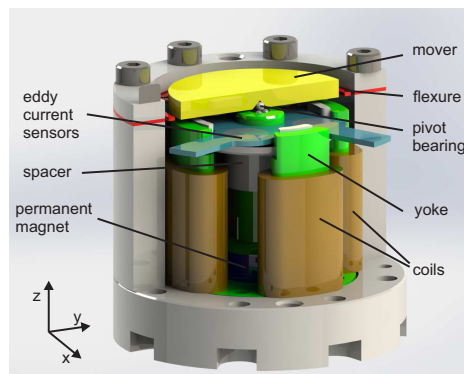


Figure 2: CAD rendering of the compact FSM system. The mover (yellow) with the mirror rests on a pivot bearing and is suspended by a mechanical flexure (red). It is actuated via one rotational hybrid reluctance actuator per axis. The eddy current sensors (light blue) measure the position in tip and tilt.

and the supporting structure for mounting the various components. The actuation system comprises the ferromagnetic yoke parts (green), the permanent magnet (blue) and the actuator coils (brown). The ferromagnetic mover (yellow), which can carry the mirror component, rests on top of a pivot bearing structure, which determines the point of rotation and is suspended by a metallic flexure (red) that constrains the non-actuated degrees of freedom. For measuring the position of the mover in tip and tilt an eddy current based sensor system (light blue) is employed, which is placed directly behind the mover and is mounted to the support structure. The non-ferromagnetic spacer (white) is used for alignment of the components and adds additional stiffness in radial direction to the top of the actuator structure.

2.2. Hybrid Reluctance Actuator with Two Degrees of Freedom

In Fig. 3 a cross section view of the FSM system is shown, illustrating the working principle of the HR actuator. As the system also employs two sources of magnetic flux, it is also termed hybrid. The DC biasing

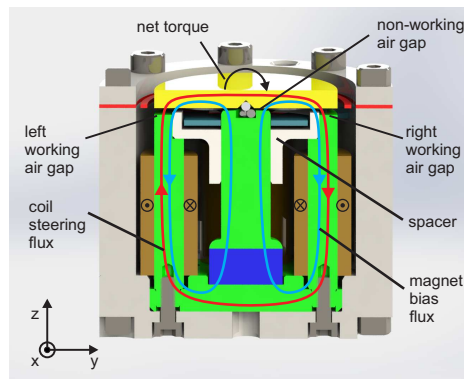


Figure 3: Concept of the rotational hybrid reluctance actuator. The ferromagnetic circuit (green), including the mover (yellow), is biased by a constant flux (light blue) from the permanent magnet (blue). The steering flux (red) generated by the coils (orange) weakens and strengthens the flux in the left and right air gap, respectively, generating a clockwise torque.

flux of the permanent magnet (blue line) passes through the center yoke part (green) and the non-working air gap and returns via the mover (yellow), the working air gaps and the outer yoke parts (green). To generate a torque on the mover, a current is applied to the actuator coils (brown), which are wired anti-parallel, and generate a steering flux, depicted by the red line, which passes through the outer yoke parts, the working air gaps and the mover in clockwise direction. As the permanent magnet represents a high reluctance for the steering flux, the center yoke part remains field free with respect to the steering flux. The steering flux has the same and opposing direction as the biasing flux in the right and left air gap, respectively, and strengthens and weakens the magnetic field in the air gaps accordingly. This results in a larger attractive force in the right air gap and a clockwise torque on the mover. By reversing the current direction a counter-clockwise torque can be generated. The torque on the mover can be calculated from the difference of the squared fluxes [22]

$$T_A = \frac{\Phi_r^2 - \Phi_l^2}{2\mu_0 A_p} \cdot r_F, \quad (1)$$

with $\Phi_{r,l}$ being the fluxes in the right and left air gap, μ_0 the permeability of vacuum, A_p the cross section of the air gap and r_F the lever arm. To actuate both rotational degrees of freedom, two rotational HR actuators are arranged perpendicular to each other, sharing the same biasing magnet and representing a single magnetic circuit. More detailed information on the actuator modeling is provided in [22].

The permanent magnet is used to linearize the motor constant, without the need to generate the biasing flux with the actuator coils, which would degrade the energy efficiency of the actuator [25]. This, however,

100 makes the actuation scheme open-loop unstable [22], which is due to the negative stiffness introduced by the permanent magnet. With no coil current applied, the flux distribution of the biasing flux solely depends on the mover position. In the middle position the biasing flux is distributed equally over both air gaps, but with the slightest displacement the flux will increase in the shorter air gap leading to an increasing torque towards the initial displacement.

105 2.3. Actuator Design

Besides the number of coil turns and the length of the working air gaps, the magnet properties have a strong influence on the motor constant. An approximated expression for the actuator torque from (1) in the middle position is found by [22]

$$T_A|_{midPos} \approx 2N i_c \cdot H_c \frac{l_m}{l_m + l_n} \cdot \frac{\mu_0 A_p}{4l_{w0}} \cdot r_F, \quad (2)$$

110 with N being the number of coil turns, i_c the coil current, H_c the coercivity and l_m the length of the magnet, l_n the length of the non-working air gap and l_{w0} the length of the working air gaps in the middle position. The simplified relation for the torque shows also that the actuator torque is linear with respect to the coil current, which is a direct result of the biasing flux of the permanent magnet.

The working air gaps and the non-working air-gap have a length of $l_{w0} = 0.75$ mm and $l_n = 0.25$ mm in the middle position of the mover, respectively, to achieve the targeted angular range. The permanent magnet (NeFeB) has a diameter of 8 mm, a height of $l_m = 4$ mm and a flux density of 1.25 T and is sized to bias the outer ferromagnetic yoke parts to about 40% of the value of the saturation flux density.

In Fig. 4 the resulting torque curves of a FEM simulation (Ansys Electronics Desktop, Ansys Inc., PA, USA) are shown for various displacement angles and current values from -6 A to 6 A. The torque curves are

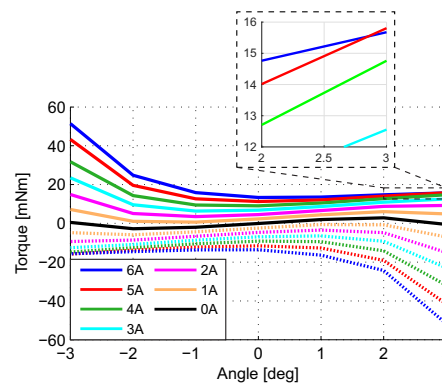


Figure 4: Simulation of torque curves with mechanical flexure. The resulting torque on the mover is shown in dependence of the applied coil current (dashed lines for negative currents) and angular position. The positive stiffness of the flexure is used to compensate the negative actuator stiffness.

120 already superimposed with the torque of the restoring mechanical flexure from the following section. For larger displacements an increasing position dependency of the torque to current ratio is observable, which is due to increased biasing flux values when the mover is closer to the yoke parts. At 6 A the actuator generates less torque at a displacement of 3° than at 5 A (see zoomed figure). This is because the steering flux from the actuator coils already exceeds the DC biasing flux, such that the resulting flux density vector changes its direction in the air gap where magnet bias and coil steering flux have opposing directions. This reduces the difference of the squared fluxes in (1), leading to a reduced torque.

125 Considering the impedance of the actuator, which is increasing at higher frequencies due to its inductance, a tradeoff between a high current (smaller N) and a high voltage (larger N) application has to be made

with regard to the capabilities of the applied amplifier, when defining the number of coil turns. A high current application has a lower number of coil turns, entailing a smaller inductance, and requires a higher current at the cost of a smaller terminal voltage. A high voltage application has a higher number of coil turns, entailing a larger inductance, and requires a smaller current at the cost of a higher terminal voltage provided by the amplifier. The compact FSM is designed as high current application, due to the availability of respective amplifier designs, with 45 turns per coil (0.4 mm^2 wire), determined by the available space.

Parasitic dynamics due to eddy currents in the ferromagnetic yoke parts cause an additional phase lag, which increases towards higher frequencies, and can limit the achievable closed-loop bandwidth [26]. As a layered yoke design is not possible and optimized yoke cross sections and shapes are required due to the small system dimensions, common yoke materials are not applicable. To maximize the motor constant, which is related to the maximum values of magnetic flux, further a material with high saturation flux density is required to guide large magnetic flux in a small volume. After a review of materials the non-commonly used *Vacoflux 50* (Vacuumschmelze GmbH, Germany) is chosen due to its high saturation flux density of 2.35 T and its comparably high specific electric resistance ($0.4 \mu\Omega\text{m}$), which reduces eddy currents in the yoke parts induced by the changing magnetic field. Simulations and analysis showed that due to the material choice and the compact yoke dimensions (cross section of 12 mm^2 with aspect ratio of 2.2:1) the phase lag is not as severe as in actuators with larger yoke dimensions and is about 25° at 1 kHz (data not shown). To enable manufacturing of the yoke and the coils, the yoke is designed and manufactured piece-by-piece in 5 individual parts - 4 coil bodies and one center part - and assembled thereafter.

In summary guidelines for the actuator design can be formulated as follows:

- Derive air gaps required for desired angular range.
- Size magnet to bias the magnetic circuit with a flux density of about 40% of the saturation flux density.
- Choose length of the magnet l_m at least a factor 10 larger than the length of the non-working air gap l_n , to neglect influence on the motor constant (see (2)).
- Define number of coil turns to generate the biasing flux at the maximum admissible current to obtain the maximum torque.
- Balance the tradeoff between coil turns and inductance according to the amplifier properties.
- Use FEM simulation to investigate if phase lag requires layered yoke parts.

2.4. Mechanical Suspension System

The mechanical suspension system is crucial to obtain well shaped system dynamics that enable an effective closed-loop control and a high system performance. The suspension system is required to (i) restrict the non-actuated degrees of freedom (high stiffness), (ii) enable well-decoupled motion in the actuated degrees of freedom (low stiffness) and (iii) place its structural modes well above the targeted crossover frequency, in order to increase the stability margins of the system. In the particular case of the HR actuator the suspension system also needs to (iv) be capable to react the large offset forces on the mover in vertical direction (8.2 N at 0 A, 9.4 N at 6 A), which are caused by the permanent magnet and (v) to be non-ferromagnetic to avoid increased flux leakage. A flexure based suspension structure showing the second and the fourth property is, however, hardly feasible. For this reason the suspension system consists of a flexure mechanism and a pivot bearing.

The flexure mechanism enables rotational motion around x- and y-axis and restricts translational motion along these axes as well as rotational motion around the z-axis. It is designed to slightly overcompensate the negative actuator stiffness in order to make the system open-loop stable and has a rotational stiffness of $k_f = 5.7 \text{ mNm/deg}$ (325.6 mNm/rad). To maximize the length of the flexure legs within the small system dimensions, for the sake of a large range of elastic deformation, the four flexure legs span circular sectors of 90° around the circular mover. With the mover dimensions fixed and the dimensions of the base structure given, the space and thus the maximum width of the flexure legs is strictly limited to obtain a sufficient level of stiffness. An FEM simulation guided design reveals, that this makes typical flexure materials like

175 aluminium not applicable, as the desired range of elastic deformation (elastic range of e.g. aluminium only about 1.5°) can not be obtained for the desired stiffness value. For this reason titanium, which has with 930 MPa a yield strength that is e.g. 3.3 and 4.5 times larger as compared to aluminium and stainless steel, respectively, is chosen as flexure material, yielding a significantly higher safety factor and elastic range. The obtained flexure has a leg width of only 0.75 mm and a thickness of 0.4 mm. To guarantee small
180 manufacturing tolerances the flexure is wire cut from a 0.4 mm titanium sheet. According to a modal analysis with ANSYS (Ansys Inc., PA, USA) the flexure shows a first structural mode (bending of the flexure legs) around 6 kHz, which is well above the target crossover frequency. Fig. 5 shows the bottom side of the flexure together with the bonded 20 mm diameter mover. The first structural mode of the mover occurs well above 20 kHz.

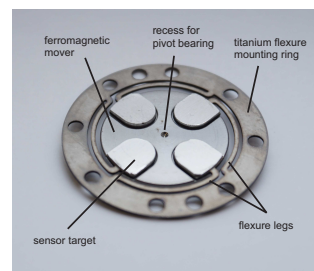


Figure 5: Integrated mover with flexure. The bottom side of the ferromagnetic mover with the recess for the pivot bearing and the titanium flexure is shown. Aluminium targets for the eddy current sensors are also depicted.

185 Fig. 4 shows the simulation results of the actuator torque superimposed with the torque generated by the restoring flexure, resulting in a system with a slightly positive stiffness at small displacements. At displacements larger than 2° the negative stiffness dominates again, leading to a snap-in of the mover to the yoke parts when operated in open-loop.

For reacting the high forces in vertical direction, in order to avoid damaging the flexure, and for fixing the point of rotation of the mirror, the mover has a recess on the bottom (see Fig. 5) and rests on a pivot bearing. A simple ball bearing using a single sapphire ball, as used in [22], has the drawback of a comparably large contact area and a higher friction coefficient between ball and the mover or the stator, respectively. This increases wear and reduces the lifetime of the bearing. To decrease wear during operation, the simple ball bearing is replaced by a pyramid like structure (cf. Fig. 3) of four individual balls. With the bottom
190 balls bonded to the stator and the upper ball bonded to the recess of the mover, this reduces the contact area to three points on the surface of the balls for rotational movement. It further fixes the center of rotation in the center of the upper ball and locates it only 3 mm behind the mirror surface. Instead of sapphire balls, the pivot bearing comprises four siliconnitride (Si₃N₄) balls with a diameter of 1 mm. Properties of Si₃N₄ include high strength, a small Young's modulus and a small thermal expansion coefficient, which makes them well suited for bearing designs. As there is only motion between the Si₃N₄ balls, also the friction
195 coefficient is reduced.

2.5. Position Sensor System

For enabling the mounting of a mirror onto the mover and to make use of its entire aperture, the position sensor system needs to be integrated below the mover. To obtain the required level of integration,
205 eddy current sensors are chosen, which can be manufactured in arbitrary and compact shapes and directly integrated into an anorganic carrier material (embedded coil technology) [27]. Apart from the required level of compactness and precision, these sensors offer long-term stability, mechanical robustness and high temperature capabilities. The resulting geometry of the sensor ceramic has four mounting legs (cf. Fig. 2) a thickness of only 0.6 mm and four sensor coils with a diameter of 5 mm. The integrated mover offers

recesses for bonding the flexure pads to the mover and also carries the aluminium sensor targets placed 0.8 mm above the sensor coil locations. The sensor targets are also obtainable in Fig.5.

2.6. Modeled System Dynamics

The effective stiffness k_{eff} of an HR actuated system results from the superposition of the flexure stiffness k_f and the negative actuator stiffness k_a . It depends on the operating point, as the actuator stiffness k_a increases when the mover is close to the ferromagnetic yoke parts [28]. This shifts the suspension mode of the system to lower frequencies for operating points in increasing distance to the middle position. The same relation is observed between suspension mode and scan amplitude α , when operating the HR actuator in a continuously scanning mode without offset [22]. This can also be explained by an amplitude dependent changing value of the average effective stiffness $k_{eff}(\alpha)$.

In order to estimate the effect of the changing stiffness on the FSM dynamics in the scanning mode, the relative change in effective stiffness is estimated from the gradient of the simulated 0 A torque curve, shown in Fig. 4, at the angle corresponding to the respective scan amplitude. At small signal deflection ($< 0.1^\circ$) the effects of the negative actuator stiffness k_a are small, such that only the stiffness of the designed flexure k_f is relevant. The effective stiffness values $k_{eff}(\alpha)$ obtained from the torque curves can be related to the small signal stiffness k_f , resulting in the relative stiffness $k_r = k_{eff}/k_f$. With the effective stiffness values $k_{eff}(\alpha)$, the stiffness of the flexure $k_f = 325.6$ mNm/rad and the inertia of the mover with the mirror $I = 4.14 \times 10^{-5}$ g·m², estimated from the CAD tools, a parametrized second order system model

$$P(s, \alpha) = K \cdot \frac{1}{k_{eff}(\alpha)} \cdot \frac{\omega_0^2}{s^2 + 2\omega_0\zeta s + \omega_0^2}, \quad (3)$$

with $\omega_0 = \sqrt{|k_{eff}(\alpha)|/I}$, $\zeta = c/(2\sqrt{|k_{eff}(\alpha)|I})$, damping parameter $c = 0.011$ and gain $K = 40$ can be obtained. Additional dynamics due to sampling delays or eddy currents are neglected at this point.

The dynamics of the resulting system models for several scan amplitudes from 0.1 to 2.5° are depicted in Fig. 6. For the small signal case with the flexure stiffness dominating, the suspension mode is calculated

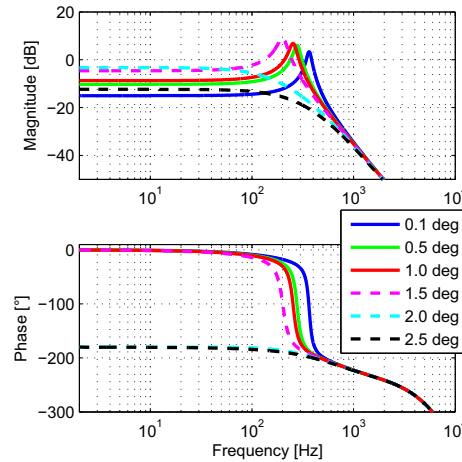


Figure 6: Modeled system dynamics with changing stiffness. The TFs of the system dynamics are evaluated at various drive amplitudes. The effective stiffness of the system is reduced towards higher amplitudes due to the increasing negative stiffness of the actuator.

to occur at 418 Hz. The spring line is shifted upwards with increasing scan amplitudes, as a consequence of the reduced effective stiffness, and the suspension mode is shifted to lower frequencies accordingly. At

amplitudes larger than or equal to 2° the resonance peak of the suspension mode vanishes and the spring line is shifted downwards again.

This can be explained by replacing s by $j\omega$ in (3), which yields

$$P(j\omega, \alpha) = K \cdot \frac{1}{k_{eff}} \cdot \frac{1}{1 - (\omega/\omega_0)^2 + j2\zeta(\omega/\omega_0)}. \quad (4)$$

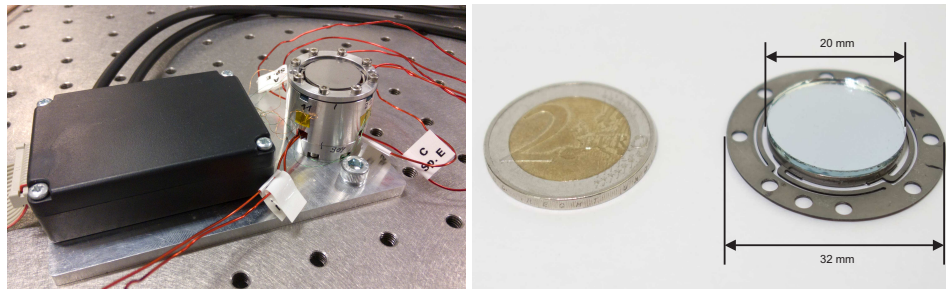
When replacing ω_0 by $\sqrt{k_{eff}(\alpha)/I}$ in the second term of the numerator it can be seen that the sign of the term depends on the sign of $k_{eff}(\alpha)$. If k_{eff} becomes negative the second term can no longer cancel the 1 at ω_0 , such that the stable pole becomes unstable and the magnitude shows well-damped low-pass characteristics, as soon as the negative actuator stiffness k_a becomes dominant. Comparing the result to Fig. 4 shows that the slope of the 0 A curve also changes its sign around angles of 2° , indicating a dominant negative effective stiffness k_{eff} . This analysis also indicates that the system with the designed flexure will be open loop stable for displacements up to around 2° . This aspect will be revisited in Section 4.1 when evaluating the closed-loop dynamics.

From a controls perspective this system behavior appears troublesome, when the system is controlled with a crossover frequency on the spring line. When, however, controlling the system with a crossover frequency on its mass line (see Section 3.3), changing dynamics do not have to be considered, as the mass line is not affected by the change in effective stiffness and also the observed torque-to-current relation is almost constant [28]. This aspect will be revisited in Section 3.2.

3. Compact FSM Prototype System

3.1. System Components

The prototype system of the compact FSM, shown in Fig. 7a, has an outer diameter of 32 mm and a height of 30 mm. Each actuator axis is driven by a custom made power amplifier (Amplifier type MP38CL, Apex Microtechnology, Tucson, AZ, USA), which are current controlled by PI controllers with a bandwidth of 30 kHz, implemented on the FPGA of a rapid prototyping platform (Type: DS1202, dSPACE GmbH, Germany). A pair of actuator coils has an inductance of 0.155 mH and a resistance of 0.113 Ω . Due to the small ohmic load the amplifier has to dissipate the majority of the required power internally, such that a preceding 5 Ω power resistor, an appropriate heat sink and a 30 V supply voltage are used to stay within the thermal limits of the amplifiers.



(a) Experimental system setup.

(b) Mover with mounted mirror.

Figure 7: Experimental system setup. (a) shows the compact FSM system prototype with mounted flexure and mover. The wires of the two pairs of actuator coils are observable, as well as the black housing of the readout electronics for the eddy current position sensors. (b) depicts the flexure with the mover and the 20 mm mirror, bonded to the mover from top. A comparison to the size of a 2 Euro coin is made.

260 To measure the mover position in tip and tilt, a custom made eddy current sensor system from Micro-Epsilon is used, which is carefully aligned with the outer housing. It has a bandwidth of 50 kHz and a resolution of $17.5 \mu\text{rad rms}$. Fig. 7a shows the assembled system prototype together with the readout electronics of the position sensor system.

265 The mover can accommodate an arbitrary optical load with a diameter equal or smaller than 20 mm, which can be bonded to the mover. For the prototype system a conventional glass mirror with a diameter of 20 mm and a thickness of 1 mm was used. Fig. 7b shows an image of the flexure with the mover and a mounted mirror, which is about as small as a 2 Euro coin. Alternatively the reflective layer can be directly attached to the mover via, e.g. vapor deposition.

270 To identify the system dynamics of the compact FSM prototype for the design of position controllers, a system analyzer (3562A, Hewlett-Packard, CA, USA) is used. The reference currents of the current control loops are considered as the system inputs, while the signals of the position sensors are considered as the system outputs.

3.2. System Identification

The small signal frequency response data of both system axes are depicted in Fig. 8. Both system

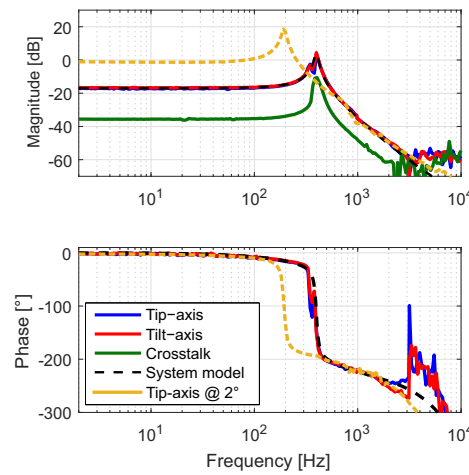


Figure 8: Measured and modeled system dynamics of the FSM system prototype at 50 mA input current. The frequency response of both system axes (blue and red) are of second order and show a resonance frequency at 400 Hz. No bandwidth limiting structural modes can be obtained. The system model (dashed black), the crosstalk magnitude (green) and the frequency response at an offset position of 2° (dashed orange) are also depicted.

275 axes (solid red; dashed blue) show similar dynamics with a suspension mode at 397 Hz, which is slightly lower than expected from the modeling in Section 2.6. The slight double-peaking is most likely caused by a slight pretension of the flexure due to mounting tolerances. There are no bandwidth limiting structural modes observable, which is in good accordance with the FEM simulation. Beyond the suspension mode the dynamics have a -50 dB slope and show an increasing phase lag towards higher frequencies. The deviation from a pure mass line is explained by eddy currents in the conductive yoke parts [26], which can be modeled by a simple lag-lead term in the frequency range of interest (see (5)). The sensor and the digital system contribute to the phase lag to a lower extent. The noise floor of the system is around -60 dB. To model the small signal dynamics of both axes, the same third order model with time delay

$$P(s) = K \cdot \frac{\omega_0^2}{s^2 + 2\omega_0\zeta_0 s + \omega_0^2} \cdot \frac{s + \omega_1}{s + \omega_2} \cdot e^{-sT_d}, \quad (5)$$

with $K = 0.141$ and parameters according to Table 2, can be used. The time delay of $T_d = 50 \mu\text{s}$ is used to model the entire time delay from amplifier input to sensor output including the phase lag of the digital system and the sensor system.

Table 2: Coefficients of the actuator system model.

Index	$\omega_{Index} [\text{rad/s}]$	ζ_{Index}
0	2.5×10^3	0.04
1	1.4×10^4	-
2	5×10^3	-

Additionally, the small signal frequency response at an offset position of 2° was measured and is also given in Fig. 8. It demonstrates that the mass line is not affected by the negative stiffness and that the motor constant also remains unchanged for larger displacements. To investigate the crosstalk between the system axes, the magnitude response of the crosstalk frequency response (green) is measured. The crosstalk magnitude response is 19 dB smaller than the magnitude of the axis response at DC and has a peak value at the resonance frequency which is 15 dB smaller than the axis response. This well decoupled behavior justifies the application of one SISO feedback controller per axis, which are designed in the next section.

3.3. Controller Design and Implementation

The position controllers $C(s)$ for both axes are designed with the aim to maximize the crossover frequency, while maintaining a phase margin (PM) of at least 20° . They represent the outer control loop around the current control loop discussed in Section 3.1. Based on the identification and the absence of structural modes a PID controller is chosen and tuned for a crossover frequency of 900 Hz [29]. The P-gain shifts the loop gain to intersect the 0 dB line at the targeted crossover frequency, while the D-gain generates a phase lead and the I-gain (stopped below 1 Hz) is used to reduce the steady state error by increasing the loop gain at low frequencies. To limit the controller gain at high frequencies, the D-action is stopped by a pole at 4.2 kHz.

The resulting controller reads as

$$C(s) = K_C \cdot \frac{(s^2 + 2\zeta_{z_1}\omega_{z_1}s + \omega_{z_1}^2)}{\left(\prod_{i=1}^2 s + \omega_{p_i}\right)}, \quad (6)$$

with a gain $K_C = 174.4$ and coefficients according to Table 3. As the frequency responses of both system axes are similar, the same controller can be applied. For implementing the controllers in the processor of the dSPACE system they are discretized for a sampling frequency of $f_s = 40 \text{ kHz}$ by using Pole-Zero-Matching [30].

Table 3: Coefficients of the PID controller.

Index	$\omega_{Index} [\text{rad/s}]$	ζ_{Index}
z_1	1.85×10^3	0.652
p_1	6.28	-
p_2	2.64×10^4	-

4. Evaluation of System Performance

To evaluate the performance of the compact FSM, the closed-loop system dynamics, the tracking performance and the operation limits are investigated.

4.1. System Dynamics

The measured loop gain of the tip axis (black) and the complementary sensitivity function of the tip (blue) and tilt-axis (red) of the compact FSM prototype with the designed feedback controller are shown in Fig. 9. The loop gain has a crossover frequency of $f_c = 900$ Hz, a PM of 21° and a gain margin (GM) of 8 dB. The complementary sensitivity functions of the closed-loop system with both system axes controlled have a -3 dB bandwidth of 1.5 kHz and 1.6 kHz, respectively, with a comparable gain peak of 4.2 dB around 1 kHz. The controller actively dampens the resonance of each axis in the closed loop, significantly reducing the excitation of the respectively other axis and therewith the crosstalk [31]. The increased loop gain at the resonance additionally increases the disturbance rejection capability of each axis, compensating crosstalk, which is essentially an external disturbance, particularly well in this frequency range.

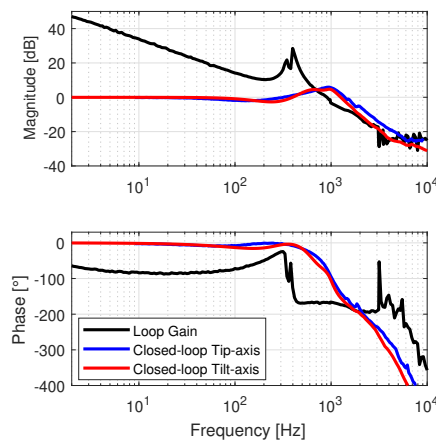


Figure 9: Verification of controller design. The measured loop gain (black) and the complimentary sensitivity function of the tip (blue) and tilt-axis (red) of the closed-loop system with the designed controller C are shown. The open loop frequency response has a PM and GM of 20° and 8 dB, respectively. The closed-loop system axes show a -3dB bandwidth of 1.5 kHz and 1.6 kHz, respectively.

To investigate the change of system dynamics dependent on the scan amplitude, the sensitivity function of the closed-loop system

$$S(s) = \frac{1}{1 + P(s)C(s)} \quad (7)$$

is measured at various amplitudes and depicted in Fig. 10a. For frequencies well below the crossover frequency f_c the loop gain $P(s)C(s)$ is large with respect to the 1 in the denominator, such that, as $C(s)$ remains unchanged, a change in the plant dynamics becomes directly observable in the sensitivity function. As for the simulated system dynamics in Fig. 6, the suspension mode, appearing as a notch in the sensitivity function, shifts to lower frequencies and is increasingly damped for increasing scan amplitudes. The spring line shifts up accordingly, which increases the loop gain and shifts the slope of $S(s)$ to lower values accordingly. For large scan amplitudes of 2° and 2.5° the effective stiffness k_{eff} becomes negative, such that there is no notch in the frequency response of $S(s)$ anymore and the slope of $S(s)$ starts to shift to higher values again, as the absolute value of k_{eff} is increasing. Fig. 10b shows a comparison of the relative stiffness values k_r , as ratio of the effective and the flexure stiffness, k_{eff}/k_f for various scan amplitudes. The stiffness values obtained from the measurements of the sensitivity function $S(s)$ and the control sensitivity function $U(s) = C(s)/(1 + C(s)P(s))$ (solid and dashed blue) are depicted, which show good agreement with the relative stiffness values estimated from the simulation results (solid red) in Fig. 4. For scan amplitudes

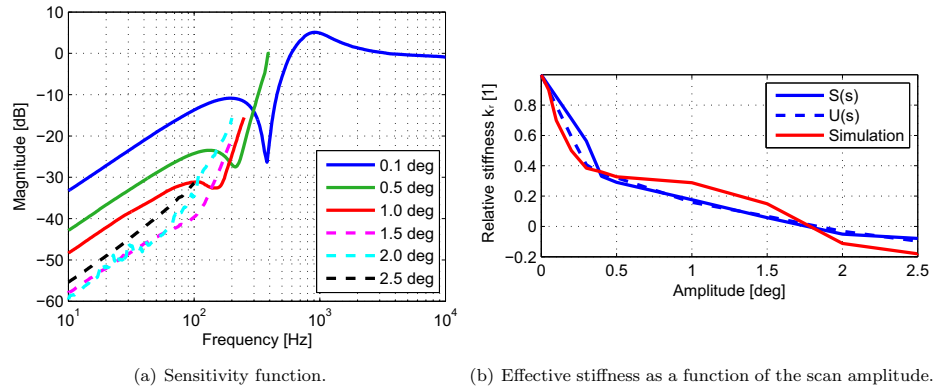


Figure 10: Variation of effective stiffness in dependence of scan amplitude. (a) shows the sensitivity function of the system measured at various scan amplitudes. With increasing amplitude the stiffness is reduced. (b) depicts the stiffness variation relative to the small signal value for $S(s)$ and $U(s)$ compared to the simulated stiffness variation relative to the designed flexure stiffness.

larger than 1.5° the effective stiffness becomes negative, which entails an open-loop unstable system at large scan amplitudes.

4.2. Tracking Performance

In order to investigate the tracking performance of the compact FSM prototype, various trajectories have been tested. In Fig. 11a dual axis operation is demonstrated by showing the result of tracking a Lissajous trajectory [32] with fundamental frequencies of 40 Hz and 30 Hz and a scan amplitude of 2.5°. The areal rms tracking error, which is evaluated for each sampled point on the trajectory, is 1.4 mdeg (25μrad). To demonstrate the applicability of the developed FSM for beam steering operations within an optical system, it is integrated into a laser projection system. Fig. 11b shows the projection of the Lissajous trajectory on a CMOS sensor, placed in a distance of 91 mm parallel to the mirror plane. Due to the alignment, an almost quadratic scan area of about 15.9 x 15.9 mm is obtained at a mechanical scan amplitude of 2.5°.

In Fig. 12a the fast scan axis of the compact FSM is shown while tracking a raster trajectory with 30 Hz fast axis and 0.5 Hz slow axis frequency and a scan amplitude of 3°. Higher fundamental frequencies of the triangular reference signal at maximum amplitude would already result in distorted position signals at the output, caused by the current limitation. The peak-to-valley and the rms tracking error are 0.18° (3.2 mrad) and 0.031° (0.54 mrad), respectively. For demonstrating that the control performance is not affected by the changing plant dynamics the rms tracking error for the raster trajectory is evaluated at various scan amplitudes. The results are given in Table 4 showing that the relative error, i.e. the error related to the scan amplitude, is between 1-3% for all tested amplitudes.

To evaluate the angular resolution of the closed-loop system, a step signal with a step height of 4 mdeg, shown in Fig. 12b, is used. The rms positioning uncertainty results to 2 mdeg (34μrad), such that the 4 mdeg steps are still well observable.

4.3. Operation Limits

For investigation of the operation limits of the closed-loop controlled compact FSM, the safe operation area, describing the feasible amplitude/frequency combinations, is determined by applying a sinusoidal reference signal to one system axis. The frequency of the reference signal is varied between 1 Hz and 1.5 kHz and the amplitude is maximized at each frequency point until either the mechanical or the current limit is reached (data not shown). Measurements reveal that the system can be operated with the maximum scan

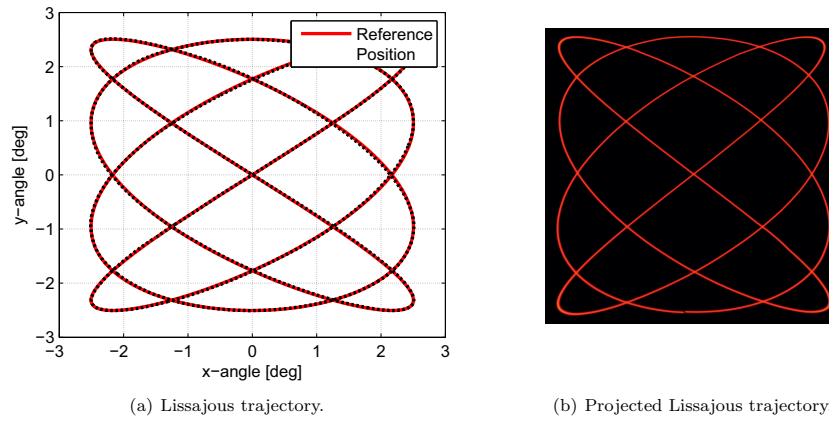


Figure 11: Measured dual axis operation. (a) demonstrates dual axis operation by tracking a Lissajous trajectory with frequencies of 40 and 30 Hz at a scan amplitude of 2.5° . (b) Lissajous trajectory projected by a laser projection system comprising the designed FSM. The trajectory is recorded by a CMOS sensor in a distance of 91 mm.

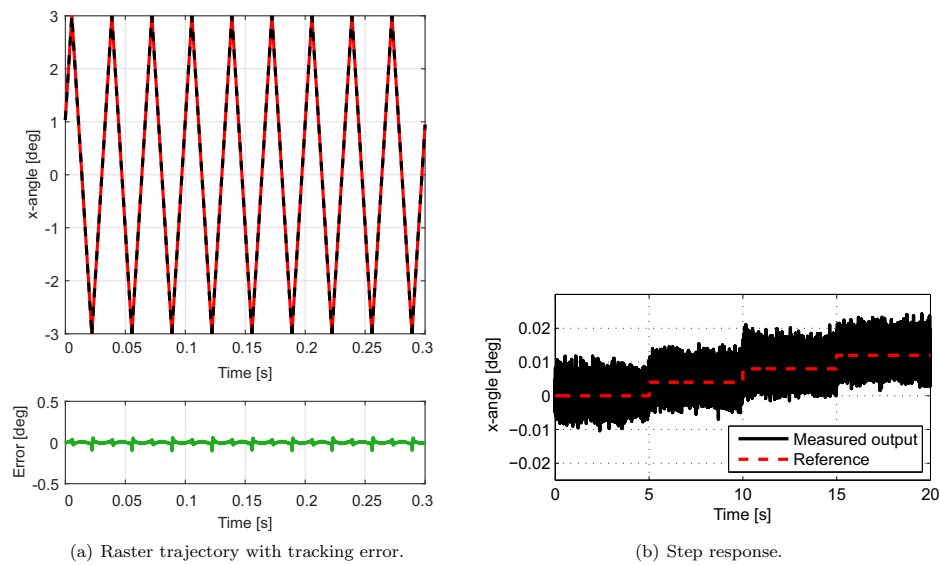


Figure 12: Measured tracking performance and resolution. (a) depicts the fast scan axis of the system tracking a raster trajectory with the maximum scan amplitude of 3° and fundamental frequencies of 30 and 0.5 Hz. (b) shows the response to steps of 4 mdeg. The remaining rms positioning uncertainty results to 2 mdeg ($34 \mu\text{rad}$).

Table 4: Tracking error of raster trajectory at various scan amplitudes.

Amplitude [deg]	RMS tracking error [deg]
0.1	0.003
0.5	0.008
1	0.014
1.5	0.018
2	0.023
2.5	0.026
3	0.031

amplitude of ± 52.4 mrad ($\pm 3^\circ$) up until around 200 Hz. Above this frequency the admissible maximum
 365 amplitude continuously decreases towards higher frequencies. At 1.5 kHz the system can still be operated
 with a scan amplitude of 0.6 mrad, which equals a maximum acceleration of 5.3×10^4 rad/s², clearly
 exceeding the initially targeted value of 4×10^4 rad/s².

In summary it is shown that the designed highly compact FSM system, based on an integrated HR
 370 actuator design, provides a high bandwidth of 1.5 kHz and an angular range of $\pm 3^\circ$ in two system axes,
 satisfying or even exceeding the initial performance goals, while also complying with the compact dimensional
 requirements.

5. Discussion and Conclusion

In this paper a novel compact and highly integrated FSM system is presented, which relies on a 2DoF
 HR actuator, a suspension system comprising a titanium flexure and a customized eddy current based sensor
 375 solution. The actuation is based on an HR force concept using one permanent magnet to generate a biasing
 field for both system axes and two coil pairs to generate individual steering fluxes. The system provides
 an angular scan range of ± 52.4 mrad ($\pm 3^\circ$) in both rotational degrees of freedom up to 200 Hz, while
 having a small signal closed-loop bandwidth of 1.5 kHz for both system axes. The FSM system is with
 dimensions of $\varnothing 32 \times 30$ mm significantly smaller than HR actuated systems reported in literature so far
 380 having dimensions of $\varnothing 100 \times 70$ mm [22] and $65 \times 65 \times 40$ mm [19], respectively, which equals a volume
 reduction around one order of magnitude. A further substantial miniaturization of the presented FSM
 system concept would, however, lead to increased stray flux within the actuator due to shorter distances
 between yoke parts and unfeasible flexure dimensions, such that the achieved dimensions can be considered
 close to the lower feasible dimensional limit of the proposed design. The angular range and the positioning
 385 uncertainty of the closed-loop system of $34 \mu\text{rad rms}$ is comparable to large range voice coil FSMs. With
 a product of range times bandwidth, serving as measure for the system performance, of 157.2 mrad·Hz the
 compact FSM also outperforms typical reported reluctance (104 mrad·Hz) [22], voice coil (61 mrad·Hz) [7]
 and piezo (12 mrad·Hz) [5] actuated systems with respect to system performance. Due to the high level
 of compactness there is a wide variety of potential applications for the proposed FSM system, including
 390 compact scanning units for optical systems, systems for tip/tilt correction in telescopes and systems for line
 of sight stabilization within optical communication devices.

Acknowledgment

The financial support by the Austrian Federal Ministry for Digital, Business and Enterprise, and the
 National Foundation for Research, Technology and Development, as well as MICRO-EPSILON MESSTECH-
 395 NIK GmbH & Co. KG and ATENSOR Engineering and Technology Systems is gratefully acknowledged.

References

- [1] H. Yoo, M. E. van Royen, W. A. van Cappellen, A. B. Houtsmuller, M. Verhaegen, G. Schitter, Automated spherical aberration correction in scanning confocal microscopy, *Review of Scientific Instruments* 85 (2014) 123706.
- [2] Q. Zhou, P. Ben-Tzvi, D. Fan, A. A. Goldenberg, Design of fast and steering mirror and systems for precision and laser beams and steering, *IEEE International Workshop on Robotic and Sensors Environments*, Ottawa, CAN (2008).
- [3] L. R. Hedding, R. A. Lewis, Fast steering mirror design and performance for stabilization and single axis scanning, *SPIE Vol. 1304 Acquisition, Tracking and Pointing IV* (1990) 14–24.
- [4] M. Hafez, T. Sidler, R. Salathe, G. Jansen, J. Compter, Design and simulations and experimental and investigations of a compact single mirror tip/tilt laser scanner, *Mechatronics* 10 (2000) 741–760.
- [5] H. F. Mokbel, W. Yuan, L. Q. Ying, C. G. Hua, A. A. Roshdy, Research on the mechanical design of two-axis fast steering mirror for optical beam guidance, *Proceedings of 2012 International Conference on Mechanical Engineering and Material Science (MEMS 2012)* (2012).
- [6] M. Guelman, A. Kogan, A. Livne, M. Orenstein, H. Michalik, Acquisition and pointing control for inter-satellite laser communications, *IEEE Transactions on Aerospace and Electronic Systems* 40 (2004) 1239.
- [7] S. Xiang, P. Wang, S. Chen, X. Wu, D. Xiao, X. Zheng, The research of a novel single mirror 2d laser scanner, *Proc. of SPIE* 7382 (2009).
- [8] S. Shao, Z. Tian, S. Song, M. Xua, Two-degrees-of-freedom piezo-driven fast steering mirror with cross-axis decoupling capability, *Review of Scientific Instruments* 89 (2018).
- [9] N. H. Vrijsen, J. W. Jansen, E. A. Lomonova, Comparison of linear voice coil and reluctance actuators for high-precision applications, *Power Electronics and Motion Control Conference (EPE/PEMC)* (2010).
- [10] A. van Lievennoogen, A. Toma, U. Ummethala, Challenges in the application of hybrid reluctance actuators in scanning positioning stages in vacuum with nanometer accuracy and mgauss magnetic stray field, *American Control Conference* (2013).
- [11] A. Katalenic, Control of reluctance actuators for high-precision positioning, Ph.D. thesis, Tu Eindhoven, 2013.
- [12] I. MacKenzie, D. L. Trumper, Real-time hysteresis modeling of a reluctance actuator using a sheared-hysteresis-model observer, *IEEE/ASME Transactions on Mechatronics* 21 (2016) 4–16.
- [13] E. Ramirez-Laboreo, C. Sagues, Reluctance actuator characterization via fem simulations and experimental tests, *Mechatronics* 56 (2018) 58–66.
- [14] S. K. et al., High bandwidth and compact fine steering mirror development for laser communications, *Proc. ESMATS 2017*, Hatfield, UK (2017).
- [15] D. Laro, R. Boshuizen, J. Dams, J. van Eijk, Linear hybrid actuator for active force cancellation, *International Symposium on Linear Drives for Industry Applications* 8 (2011).
- [16] X. Lu, Electromagnetically-driven ultra-fast tool servos for diamond turning, Master's thesis, Massachusetts Institute of Technology (2005).
- [17] D. Wu, X. Xie, S. Zhou, Design of a normal stress electromagnetic fast linear actuator, *IEEE Transactions on Magnetics* 46 (2010) 1007–1014.
- [18] J. Kim, J. Chang, A new electromagnetic linear actuator for quick latching, *IEEE Transactions on Magnetics* 43 (2007) 1849–1852.
- [19] D. J. Kluk, M. T. Boulet, D. L. Trumper, A high-bandwidth, high-precision, two-axis steering mirror with moving iron actuator, *Mechatronics* 22 (2012) 257–270.
- [20] M. Boulet, Design of a small fast steering mirror for airborne and aerospace applications, Master's Thesis, Massachusetts Institute of Technology (2008).
- [21] Y. Long, C. Wang, X. Dai, X. Wei, S. Wang, Modeling and analysis of a novel two-axis rotary electromagnetic actuator for fast steering mirror, *Journal of Magnetics* 19 (2014) 130–139.
- [22] E. Csencsics, J. Schlarp, G. Schitter, High performance hybrid-reluctance-force-based tip/tilt system: Design, control and evaluation, *IEEE Transactions of Mechatronics* 23 (2018).
- [23] E. Csencsics, S. Ito, J. Schlarp, G. Schitter, System integration and control for 3d scanning laser metrology, *IEEE Transactions on Industrial Applications* 8 (2018).
- [24] P. Grenfell, A. Aguilar, K. Cahoy, M. Long, Pointing, acquisition, and tracking for small satellite laser communications, *AIAA/USU Conference on Small Satellites, Advanced Concepts I* (2018).
- [25] R. M. Schmidt, G. Schitter, A. Rankers, J. van Eijk, *The Design of High Performance Mechatronics*, 2nd ed., Delft University Press, 2014.
- [26] E. Csencsics, J. Schlarp, G. Schitter, Bandwidth extension of hybrid reluctance force based tip/tilt system by reduction of eddy currents, *IEEE International Conference on Advanced Intelligent Mechatronics (AIM)* (2017).
- [27] M. Wasmeier, J. Hackl, S. Leveque, Inductive sensors based on embedded coil technology for nanometric inter-segment position sensing of the e-elt, *Ground-based and Airborne Telescopes V* 9145 (2014) 91451R.
- [28] S. Ito, S. Troppmair, B. Lindner, F. Cigarini, G. Schitter, Long-range fast nanopositioner using nonlinearities of hybrid reluctance actuator for energy efficiency, *IEEE Transactions on Industrial Electronics* 66 (2018) 3051–3059.
- [29] E. Csencsics, G. Schitter, Parametric pid controller tuning for a fast steering mirror, *IEEE Conference on Control Technology and Applications* (2017) 1673–1678.
- [30] G. F. Franklin, D. J. Powell, M. L. Workman, *Digital Control of Dynamic Systems*, Prentice Hall, 1997.
- [31] S. Kuiper, G. Schitter, Active damping of a piezoelectric tube scanner using self-sensing piezo actuation, *Mechatronics* 20 (2010) 656–665.

- 460 [32] E. Csencsics, R. Saathof, G. Schitter, Design of a dual-tone controller for lissajous-based scanning of fast steering mirrors, American Control Conference, Boston, MA, USA (2016).